Effects of the charge–dipole and charge–quadrupole interactions on the He+ + CO reaction rate coefficients at low collision energies

Author(s):
Martins, Fernanda B.V.; Zhelyazkova, Valentina; Merkt, Frédéric

Publication date:
2022-11

Permanent link:
https://doi.org/10.3929/ethz-b-000580726

Originally published in:
New Journal of Physics 24(11), https://doi.org/10.1088/1367-2630/ac8a0b

Funding acknowledgement:
200478 - Precision measurements with cold molecules: Rydberg states, ions and photoionization (SNF)
743121 - Cold Ion Chemistry - Experiments within a Rydberg Orbit (EC)

New Journal of Physics
The open access journal at the forefront of physics

Deutsche Physikalische Gesellschaft DPG
IOP Institute of Physics

Published in partnership with: Deutsche Physikalische Gesellschaft and the Institute of Physics

OPEN ACCESS

RECEIVED
1 April 2022

REVISED
13 July 2022

ACCEPTED FOR PUBLICATION
16 August 2022

PUBLISHED
7 November 2022

PAPER

Effects of the charge–dipole and charge–quadrupole interactions on the $He^+ + CO$ reaction rate coefficients at low collision energies

Fernanda B V Martins, Valentina Zhelyazkova and Frédéric Merkt*

Laboratory of Physical Chemistry, ETH Zurich, CH-8093 Zurich, Switzerland
* Author to whom any correspondence should be addressed.

E-mail: merkt@phys.chem.ethz.ch

Keywords: ion–molecule reaction, cold chemistry, reaction rate coefficients, Rydberg states, charge–dipole interaction, charge–quadrupole interaction, merged beams

Abstract

The reaction between He^+ and CO forming $He + C^+ + O$ has been studied at collision energies in the range between 0 and $k_B \cdot 25$ K. These low collision energies are reached by measuring the reaction within the orbit of a Rydberg electron after merging a beam of $He(n)$ Rydberg atoms and a supersonic beam of CO molecules with a rotational temperature of 6.5 K. The capture rate of the reaction drops by about 30% at collision energies below $k_B \cdot 5$ K. This behavior is analyzed in terms of the long-range charge–dipole and charge–quadrupole interactions using an adiabatic-channel capture model. Although the charge–dipole interaction has an effect on the magnitude of the rate coefficients, the effects of the charge–quadrupole interaction determine the main trend of the collision-energy dependence of the rate coefficients at low collision energies. The drop of the capture rate coefficient at low collision energies is attributed to the negative sign of the quadrupole moment of CO ($Q_{zz} = -2.839$ D Å) and is caused by the $|JM\rangle = |00\rangle$ and $|1 \pm 1\rangle$ rotational states of CO, which represent about 70% of the CO molecules at the rotational temperature of 6.5 K.

1. Introduction

In recent years, new experimental methods have been developed to study chemical reactions at very low temperatures [1–5]. Overall, this progress has been faster for studies of reactions involving neutral molecules than for studies of reactions involving charged particles, primarily because ions are easily heated by electric stray fields. Current efforts to reach temperatures below 1 K in the study of ion–molecule reactions involve the use of buffer-gas-cooled ion traps [6, 7], Coulomb crystals [8], and merged-beam techniques [9].

The rates of many fast, barrier-free ion–molecule reactions can be estimated by the Langevin capture model [10–13]. This model considers the long-range interaction between the charge of the ion and the induced dipole moment of the neutral molecule and assumes that all capture processes lead to reaction products. The Langevin capture rate constant

$$k_L = 2\sqrt{\frac{\pi^2 \alpha'(Ze)^2}{4\pi\epsilon_0 \mu}} \tag{1}$$

does not depend on the temperature or the collision energy, but only on the reduced mass μ of the reactants, the charge $q = Ze$ of the ion, and the polarizability volume α' of the neutral molecule. It represents a useful reference with which to compare calculated or experimental ion–molecule rate constants. Deviations from the Langevin rate constant can have three distinct origins: (i) the ion–molecule capture events may not all lead to the same reaction products and may even not lead to a reaction at all. (ii) The electrostatic interactions between the charge of the ion and the permanent electric dipole and

quadrupole moments of the neutral molecule can lead to pronounced departures from k_L, particularly at low temperatures, low collision energies, or in the case of state-selected reactions [12–15]. (iii) At very low temperatures, the ion–molecule capture process becomes dominated by s-wave scattering and the capture rate constants approach limiting values characteristic of the long-range potentials [16–20].

To predict reliable rate coefficients at low temperatures, the Langevin capture model has been extended to include the effects of the charge–dipole [21–24] and charge–quadrupole [18, 20, 25–27] interactions, of open-shell electronic structures of the neutral molecules [28–31], and of s-wave scattering at the lowest collision energies [20]. In selected cases, quantum-dynamical calculations that also include the short-range regions of the collisions have been performed, providing low-temperature reaction rates as well as detailed information on the role of non-adiabatic effects and on branching ratios for different product channels (see, e.g., reference [32] and references therein for the well-studied case of the $H_2^+ + H_2$ reaction).

Hardly any experimental data are available on the rate of ion–molecule reactions at temperatures T and collision energies E_{coll}/k_B below 10 K. The primary reason for the lack of experimental data in this range is the fact that ions are easily heated up by uncontrollable stray fields in the reaction volumes. We have recently developed a new method [9] to study ion–molecule reactions below 10 K, which consists of observing the reactions within the orbit of a highly excited Rydberg electron after merging a supersonic beam of the neutral molecules with a beam of Rydberg atoms or molecules using a curved, on-chip Rydberg–Stark decelerator and deflector [33]. The Rydberg electron does not influence the reaction between the ion core and the neutral molecule taking place within the Rydberg-electron orbit, but shields the reaction system from external electric fields. With this method, we have started systematic investigations at low collision energies of the role of the charge–dipole interactions with the examples of the $He^+ + CH_3F$ [34] and $He^+ + NH_3/ND_3$ [35] reactions, and of the charge–quadrupole interaction with the example of the $H_2^+ + H_2$ [36–39] and $He^+ + N_2$ reactions [40]. These studies have led to the observation of large, state-specific deviations of the rate coefficients from k_L at low collision energies.

In this article, we present the results of an investigation of the $He^+ + CO \rightarrow He + C^+ + O$ reaction at low collision energies. In a previous article, we have used this reaction system to experimentally verify that the Rydberg electron does not affect the reaction rate [41]. We observed a decrease of the reaction rate by about 30% at collision energies below $k_B \cdot 5$ K. CO has a weak permanent electric dipole moment of 0.112 D [42] and a large, negative quadrupole moment of −2.839 D Å [43]. Our motivation for this investigation was to find out whether, in this reaction system, the effects of the charge–dipole interaction, which is of longer range (R^{-2} vs R^{-3}), dominate over the effects of the charge–quadrupole interaction, despite the small dipole moment of CO. The emphasis of the article is thus placed on the investigation of the respective roles of these long-range interactions on the reaction rate at low collision energies. Most of the experimental data analyzed in this article were already presented in an earlier study of the spectator role of the Rydberg electron [41]. To facilitate the understanding, we nevertheless chose to briefly summarize the main aspects of the experimental procedure in the next section.

2. Experimental procedure

Our experimental studies of ion–molecule reactions are conducted using the merged-beam apparatus shown in figure 1, in which a supersonic beam of cold ground-state molecules and a beam of velocity-selected He Rydberg atoms are merged. When short pulses are used, the velocity dispersion taking place in the expansion reduces the range of relative velocities in the reaction volume, which improves the collision-energy resolution, as shown in previous studies of Penning-ionization reactions [44, 45].

The experimental apparatus is described in reference [35]. Here, we only outline the main features and principles of our experimental method and setup. The ion–molecule reaction $He^+ + CO \rightarrow He + C^+ + O$ is studied within the orbit of a Rydberg electron with principal quantum number n between 30 and 40, exploiting the fact that the Rydberg electron acts as a spectator and does not affect the reaction rate, as demonstrated recently [41]. We detect the ion product C^+ upon field ionization of the C(n) product of the He(n) + CO reaction.

A supersonic beam of helium atoms is produced by a cryogenic home-built short-pulse valve (valve opening time ≈20 μs) at a repetition rate of 25 Hz. After the valve orifice, an electric discharge populates the $(1s)^1(2s)^1\ ^3S_1$ metastable state, which we refer to as He^*. The He^* beam is skimmed twice before it traverses a region between two metal plates, where a laser beam ($\lambda \sim 260$ nm) excites the He^* atoms to a Rydberg–Stark state in the presence of an electric field. The He(n) atoms, with an initial velocity $v_{i,He} = 860$ m s^{-1} dictated by the temperature [(66 ± 0.1) K] of the He-beam valve, are then loaded into an electric quadrupole trap at the entrance of a curved surface-electrode Rydberg–Stark deflector and

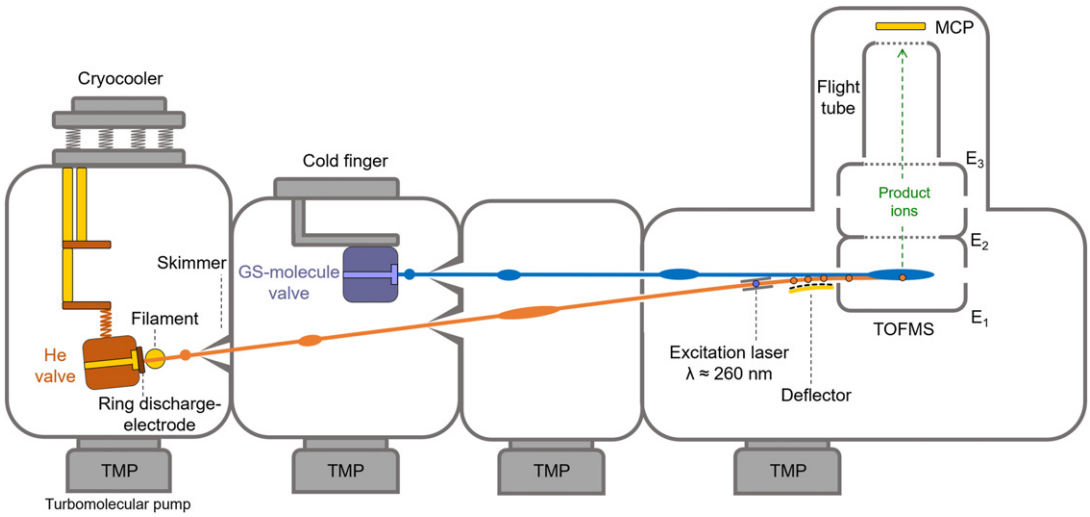

Figure 1. Schematic view of the merged-beam setup used to study the reactions of He^+ with neutral molecules at low temperatures. The ion products are detected in the time-of-flight mass spectrometer (TOFMS). See text for details.

deceleration [33, 34, 46]. We set the final velocity of the He Rydberg atoms $v_{He(n)}$ by applying time-dependent sinusoidal electric potentials to the electrodes of the deflector, as explained in references [33, 46].

The deflected He(n) beam is then merged with a supersonic beam of ground-state (GS) CO molecules, which is also generated with a temperature-stabilized home-built short-pulse valve (valve opening time ≈20 μs). The rotational temperature of the CO molecules in the beam is estimated to be (6.5 ± 1.5) K on the basis of measurements of the PFI-ZEKE photoelectron spectrum of CO recorded under similar conditions [47]. The GS-beam valve temperature is stabilized to (340 ± 1) K. The merged beams of He(n) atoms and GS molecules enter the reaction region, which is embedded in a time-of-flight mass spectrometer (TOFMS) and where the Rydberg He atoms interact with CO molecules belonging to a well-defined velocity class. A good spatial separation of the GS beam in different velocity classes is achieved because the molecules travel ∼62 cm from the GS-beam valve orifice to the region where the reaction takes place. The GS-beam valve is triggered such that the molecules traveling at a velocity v_{GS} of choice (870 m s^{-1} for the results presented below) reach the center of the reaction region at the same time as the Rydberg atoms.

We adjust $v_{He(n)}$ in the range between 710 m s^{-1} and 1200 m s^{-1} for the selected value of v_{GS} ($= v_{CO}$) and thereby vary the collision energy E_{coll} between the He Rydberg atoms and the CO molecules in the range between 0 and $\sim k_B \cdot 25$ K. The collision-energy resolution is about $k_B \cdot 200$ mK at $E_{coll} = 0$ and increases with $\sqrt{E_{coll}}$ [34]. The product ions are extracted toward a micro-channel-plate (MCP) detector at the end of the TOFMS. The TOFMS consists of three cylindrical plates (E_1, E_2, E_3) to which appropriate potentials (V_1, V_2, V_3) are applied. Monitoring the reaction products requires a good mass resolution, which is achieved by setting the potentials so that they fulfill the Wiley–McLaren conditions [48], i.e., V_1, $V_2 = \frac{1}{2}V_1$, and $V_3 = 0$. To observe the field-ionization of the reactant He(n) and detect He^+, which does not require a high mass resolution, we apply potentials as high as 5.5 kV to E_1, keeping the electrodes E_2 and E_3 grounded.

3. Experimental results

In our experiments, we monitor the reaction yield as a function of the collision energy between the reactants, as explained above. A TOF mass spectrum, averaged over 2500 experimental cycles, is recorded for each selected velocity $v_{He(n)}$ of the He-Rydberg beam. Additionally, we record TOF spectra at each value of $v_{He(n)}$ with the Rydberg-excitation laser turned off so that we can identify ions formed in Penning-ionization reactions between He^* and background-gas molecules present in the vacuum chamber. Examples of such TOF mass spectra for $E_{coll}/k_B = 6$ K are displayed in figure 2. We identify C^+ as the only product ion of the reaction between He^+ and CO, because it is the only ion formed when the Rydberg-excitation laser is turned on. To monitor the reaction yield, we integrate the C^+ ion signal

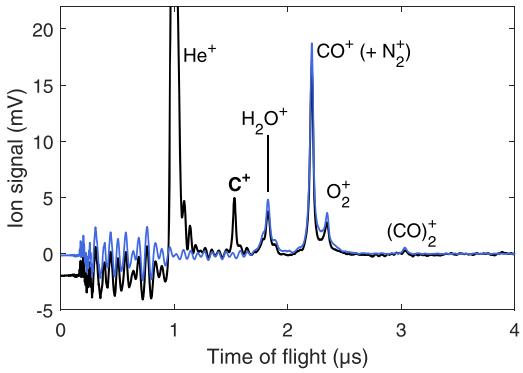

Figure 2. Time-of-flight mass spectrum of the ions detected after the reaction between He Rydberg atoms ($n = 35$) and CO molecules (black trace). The blue trace corresponds to the background signal obtained when the Rydberg-excitation laser is turned off.

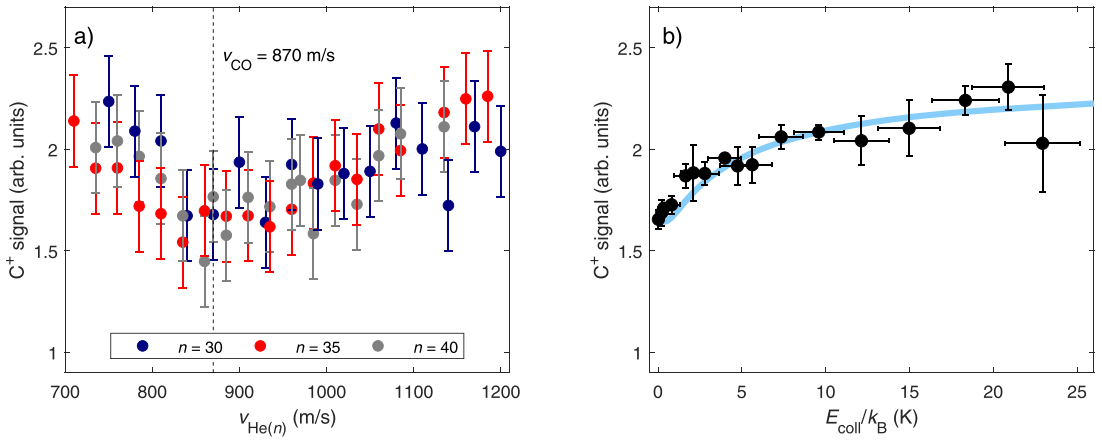

Figure 3. Integrated C^+ product signal of the reaction $He^+ + CO \rightarrow He + C^+ + O$ as a function of (a) the central velocity of the He(n) beam for a fixed value of the central CO-beam velocity $v_{CO} = 870$ m s^{-1}, indicated by the dashed line, and (b) the collision energy of the reaction. In panel (a), the blue, red and gray data points correspond to measurements carried out at $n = 30$, 35, and 40, respectively. In panel (b), the data points are averages of the data within bins corresponding roughly to half of the experimental resolution. The horizontal error bars represent the collision-energy resolution and the vertical error bars are $\pm 1\sigma$ intervals. The blue line represents the results of the calculations of the capture rate coefficients that include the charge–dipole and the charge–quadrupole interactions.

produced by field ionization and normalize it by the amount of He^+ reactant, which is estimated in a subsequent pulsed-field ionization measurement.

Figure 3 displays the integrated and normalized C^+ ion signal as a function of (a) the velocity $v_{He(n)}$ of the He(n) beam and (b) the collision energy $E_{coll} = \frac{1}{2}\mu(v_{He(n)} - v_{CO})^2$. The vertical error bars correspond to one standard deviation and the horizontal error bars to the energy resolution of our experiments, which degrades with increasing E_{coll} value [34, 35]. The experimental data used to generate figure 3 involve measurements at $n = 30$, 35, and 40, and were already reported in reference [41], where they were used to show that the state of the reactant Rydberg atom does not influence the collision-energy dependence of the reaction rate coefficients. In figure 3, we combine all data sets obtained at the different n values into a single set, which enables us to considerably improve the statistics of our measurements. The blue, red and gray data points in figure 3(a), correspond to the measurements carried out at $n = 30$, 35, and 40, respectively. To obtain the data presented in figure 3(b), the relative velocities $v_{rel} = v_{He(n)} - v_{CO}$ were converted into collision energies and the data were binned in energy intervals corresponding to roughly half of the collision-energy resolution. The black data points represent the averages within each bin and the vertical error bars the $\pm\sigma$ intervals. The horizontal error bars indicate the collision-energy resolution. These data were used as a reference with which to compare the results of calculations aiming to clarify the roles of the charge–dipole and charge–quadrupole interactions presented in section 4.

As the collision energy decreases, the C^+ product yield decreases slightly down to $\sim k_B \cdot 5$ K and more steeply at collision energies below $k_B \cdot 5$ K. At $E_{coll} = 0$, the C^+ signal is about 30% lower than that at

$E_{coll}/k_B \approx 22$ K. The trend of decreasing product yield with decreasing collision energy is similar to that observed for the $He^+ + N_2$ reaction [40]. Because N_2 does not have a permanent dipole moment, this observation suggests that the CO quadrupole moment, and not its dipole moment, determines the collision-energy dependence of the rate coefficient of the $He^+ + CO$ reaction. To verify this hypothesis, we have carried out calculations of the ion–molecule capture rate coefficients which are presented in detail in the next section.

4. Calculation of the capture rate coefficients of the $He^+ + CO$ reaction and the effects of the charge–dipole and charge–quadrupole interactions

4.1. The interaction potential between He^+ and CO

We modeled the long-range interaction between He^+ and CO as described in reference [35]. For diatomic molecules in $^1\Sigma$ electronic states, the projection of the total angular momentum vector $\vec{J}$ onto the molecular-symmetry axis is zero ($K = 0$). To describe the CO molecule, we therefore consider the molecular rotational states $i = |JM, K = 0\rangle \equiv |JM\rangle$, where J and M are the quantum numbers associated with $\vec{J}$ and its projection onto the collision axis, respectively.

The potential which describes the interaction between a molecule in the rotational state i and an ion is

$$V_i^{(\ell)}(R) = V_L^{(\ell)}(R) + \Delta E_i(R), \tag{2}$$

where $\Delta E_i(R)$ is the state-specific Stark shift and

$$V_L^{(\ell)}(R) = \frac{L^2}{2\mu R^2} - \frac{\alpha' q^2}{8\pi\varepsilon_0 R^4} \tag{3}$$

is the Langevin potential, which consists of a centrifugal and an ion-induced-dipole interaction term. In equation (3), $L = \hbar\sqrt{\ell(\ell+1)}$ is the quantized angular momentum of the collision ($\ell = 0, 1, 2, \ldots$), μ the reduced mass of the ion–molecule pair, q the charge of the ion, and $\alpha' = (\alpha'_{\parallel} + 2\alpha'_{\perp})/3$ is the average polarizability volume of the molecule ($\alpha'_{CO} = 1.953$ Å^3 [49]). The interaction arising from the CO polarizability anisotropy $\Delta\alpha' = \alpha'_{\parallel} - \alpha'_{\perp}$ ($\Delta\alpha'_{CO} = 0.532$ Å^3 [50]), which has the same selection rules as the charge–quadrupole interaction is combined with this interaction for convenience (see below).

The interaction potential in equation (2) therefore corresponds to the Langevin potential modified by a $\Delta E_i(R)$ term. This term represents the shifts that the rotational levels of CO experience as a result of the interaction between its electric multipole moments and the electric field generated by the ion.

4.2. The Stark shifts in CO induced by the charge–dipole and charge–quadrupole interaction with He^+

As a CO molecule and a He^+ ion approach, the molecular rotational levels are increasingly shifted by the electric field $F(R) = e/(4\pi\epsilon_0 R^2)$ emanating from the ion [14, 15]. To calculate the Stark shift $\Delta E_i(R)$ of the rotational levels of CO, we express the corresponding Hamiltonian matrix $\hat{H}(R)$ [35]

$$\hat{H}(R) = \hat{H}_{rot} + \hat{H}^{\lambda=1}_{Stark}(R) + \hat{H}^{\lambda=2}_{Stark}(R) \tag{4}$$

in the $|JM\rangle$ basis and determine its eigenvalues at the field corresponding to the distance R. We assign the eigenenergies $E_i + \Delta E_i(R)$ of $\hat{H}(R)$ to a J and an M value by adiabatically correlating them to the field-free $|JM\rangle$ states with rotational energies E_i at $R \to \infty$. In equation (4), $\hat{H}_{rot}$ is the rotational Hamiltonian of the molecule in zero electric field and $\hat{H}^{\lambda}_{Stark}(R)$ describes the charge–dipole ($\lambda = 1$) and charge–quadrupole ($\lambda = 2$) interactions, which mix the rotational levels of CO. Neglecting the coupling between $\vec{L}$ and $\vec{J}$, which corresponds to the centrifugal sudden approximation of reference [14], M is a good quantum number.

In the $|JM\rangle$ rigid-rotor basis set, the matrix elements of the charge–dipole interaction Hamiltonian are given by [35, 51, 52]

$$\langle J'M'|\hat{H}^{\lambda=1}_{Stark}(R)|JM\rangle = \frac{e\mu_{el}}{4\pi\epsilon_0 R^2}(-1)^M\sqrt{(2J+1)(2J'+1)}\begin{pmatrix} J & 1 & J' \\ M & 0 & -M' \end{pmatrix}\begin{pmatrix} J & 1 & J' \\ 0 & 0 & 0 \end{pmatrix}, \tag{5}$$

where μ_{el} is the permanent electric-dipole moment of the molecule and ϵ_0 the permittivity of free space. For the charge–quadrupole interaction, the matrix elements of the Stark Hamiltonian are [35, 51, 52]

$$\langle J'M'|\hat{H}^{\lambda=2}_{Stark}(R)|JM\rangle = \frac{1}{4\pi\epsilon_0}\left(-\frac{e^2\Delta\alpha'}{3R^4} + \frac{eQ_{zz}}{R^3}\right)(-1)^M\sqrt{(2J+1)(2J'+1)}\begin{pmatrix} J & 2 & J' \\ M & 0 & -M' \end{pmatrix}\begin{pmatrix} J & 2 & J' \\ 0 & 0 & 0 \end{pmatrix}. \tag{6}$$

In equation (6), the Q_{zz} component of the rank-two, traceless quadrupole-moment tensor $\mathbf{Q}$ is used to describe the quadrupole in the molecular center-of-mass reference frame ($Q_{xx} = Q_{yy} = -\frac{1}{2}Q_{zz}$ for symmetric-top and linear molecules). The charge–quadrupole interaction implies the same coupling selection rule as the anisotropic part of the charge-induced-dipole interaction, which is parameterized by the polarizability anisotropy $\Delta\alpha' = \alpha'_{\parallel} - \alpha'_{\perp}$ of the molecule, and the two terms, though of distinct origin, are treated together. The charge–quadrupole interaction is of longer range (R^{-3}) than the charge-induced-dipole interaction (R^{-4}) and typically dominates.

The charge–dipole interaction (R^{-2}) mixes rotational states of the neutral molecule according to $\Delta J = 0, \pm 1 (0 \not\leftrightarrow 0)$ and $\Delta M = 0$, whereas the charge–quadrupole interaction mixes states according to $\Delta J = 0, \pm 1, \pm 2 (0 \not\leftrightarrow 0, 1)$ and $\Delta M = 0$. The $J = 0$ state, which is isotropic and does not have a multipole moment, acquires an induced dipole moment through mixing with the $J = 1$ state via the charge–dipole interaction, and a quadrupole moment through mixing with the $J = 2$ state via the charge–quadrupole interaction. Stark states of quantum number $\pm M$ in the same J manifold are degenerate.

4.3. Rotational-state-dependent capture rate coefficients

Expressing the Stark shifts $\Delta E_i(R)$ of the CO rotational energies as a function of the ion–molecule separation, we can obtain the total interaction potentials for the $He^+ + CO$ reaction (equation (2)). From $V_i^{(\ell)}(R)$, we find the maximal angular momentum value $L_{\mathrm{max},i}$ which satisfies the Langevin-capture condition $E_{\mathrm{coll}} \geqslant V_i^{(\ell)}(R_{\mathrm{max}})$. R_{max} is the ion–molecule separation at which the potential function reaches its maximal value. The corresponding reaction cross section, $\sigma_i = \pi R_{\mathrm{max}}^2$, can be used to determine the state-specific capture rate coefficients [35]

$$k_i(E_{\mathrm{coll}}) = \frac{\pi L_{\mathrm{max},i}^2}{\sqrt{2\mu^3 E_{\mathrm{coll}}}}. \tag{7}$$

Unlike the rate coefficient resulting from a pure Langevin potential (equation (1)), the rotational-state-dependent capture rate coefficients (equation (7)) are collision-energy dependent.

The capture rate coefficient displayed as a blue line in figure 3(b) is obtained in a weighted sum over the $i = |JM\rangle$ rotational states of CO considering their probability of occupation p_i at the rotational temperature $T_{\mathrm{rot}} = 6.5$ K of the CO molecules in the supersonic beam

$$k(E_{\mathrm{coll}}) = \sum_i p_i k_i(E_{\mathrm{coll}}). \tag{8}$$

For comparison with the experimental results, we average $k(E_{\mathrm{coll}})$ over a Gaussian distribution of collision energies centered at the selected E_{coll} value (see references [34, 35] for details), which adequately describes the range of collision energies probed experimentally.

4.4. Calculation results

Figure 4 presents the results of the calculations described above, obtained following the determination of the eigenvalues of the Hamiltonian in equation (4) in a basis with $J_{\mathrm{max}} = 12$ and for electric fields corresponding to an ion–molecule separation R between 0.1 Å and 50 Å. Panels (a)–(c) display the calculated rotational-level energies of CO ($J \leqslant 2$) including their Stark shifts. The long-range adiabatic interaction potentials for the $He^+ + CO$ reaction are displayed in panels (d)–(f) and the state-specific capture rate coefficients $k_i(E_{\mathrm{coll}})$ are depicted in panels (g)–(i). The columns, from left to right, contain the results obtained considering only the charge–dipole interaction, only the charge–quadrupole interaction, and both interactions. A high-field-seeking (hfs) behavior of the rotational levels at low electric fields leads to interaction potentials that are always more attractive than the corresponding Langevin potential $V_{\mathrm{L}}^{(\ell=0)}$. Consequently, the corresponding state-specific capture rate coefficients are larger than k_{L}. Conversely, low-field-seeking (lfs) states correspond to interaction potentials which have a barrier and thus to capture rate coefficients that are lower than k_{L}. For the remainder of this article, the capture rate coefficients are reported as k/k_{L} with respect to the Langevin constant $k_{\mathrm{L}} = 1.75 \times 10^{-15}$ m^3 s^{-1} of the $He^+ + CO$ reaction.

The Stark energies of CO displayed in panels (a) and (b) of figure 4 reveal that the $|JM\rangle$ states behave very differently under the influence of the charge–dipole (a) and the charge–quadrupole (b) interaction. When only the charge–dipole interaction is considered, the $|J > 0, M = 0\rangle$ states, such as $|10\rangle$ and $|20\rangle$, are lfs. When considering the charge–quadrupole interaction only, this behavior reverses and the $|J > 0, M \neq 0\rangle$ states (e.g., $|11\rangle$ and $|22\rangle$) become lfs. Even for states which exhibit the same type of Stark

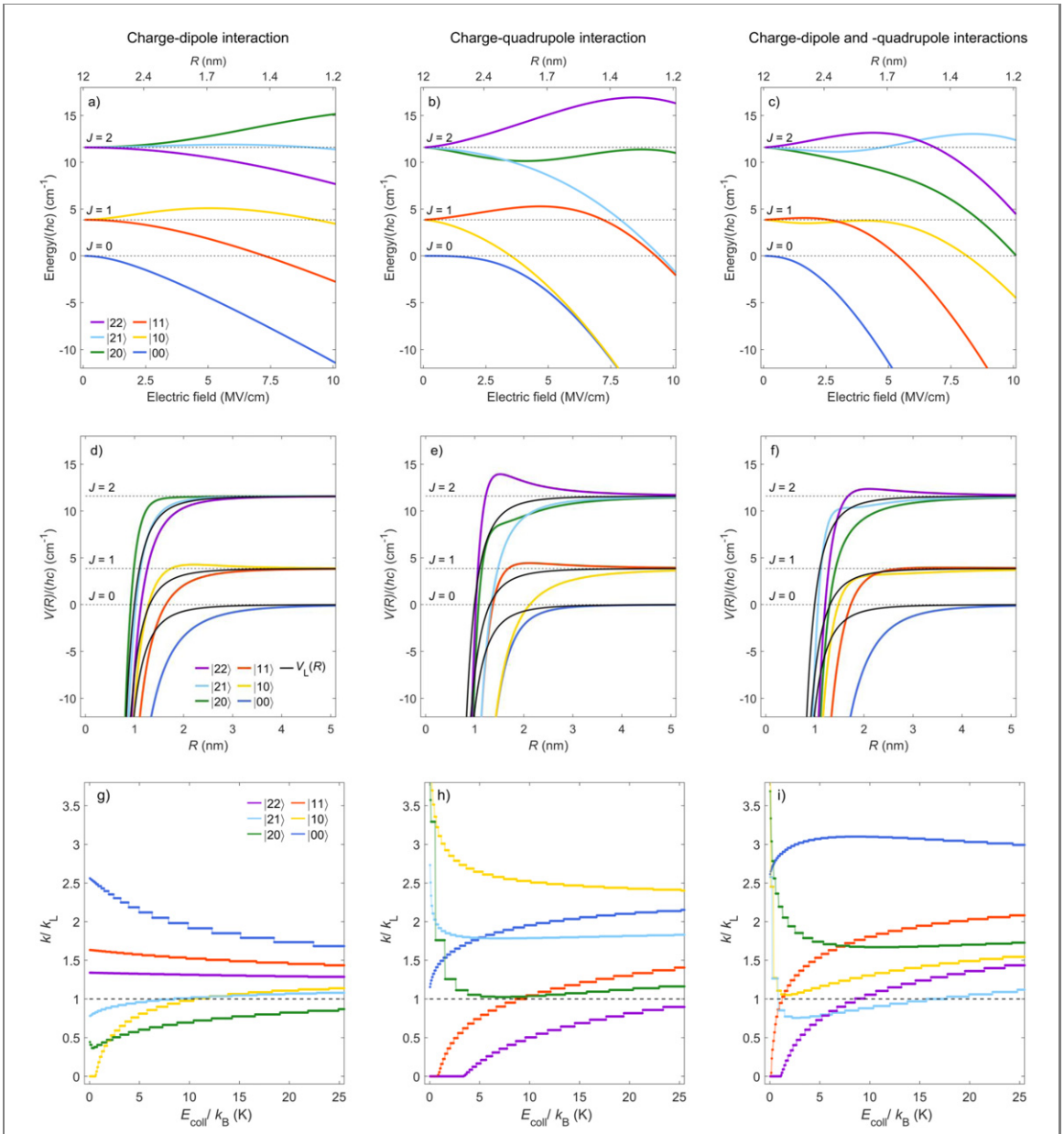

Figure 4. (a)–(c) Stark shifts of the rotational levels $|JM\rangle$ of CO with $J \leqslant 2$ in the electric field of an ion considering (a) only the charge–dipole, (b) only the charge–quadrupole interaction, and (c) both the charge–dipole and the charge–quadrupole interactions. (d)–(f) Interaction potentials for the $He^+ + CO(|JM\rangle)$ reaction, $V_i^{(\ell=0)}(R)$, for the states displayed in (a)–(c) and an s-wave collision. (g)–(i) Calculated state-specific capture rate coefficients.

shift (i.e., lfs or hfs states) when each interaction is considered separately (e.g., the hfs $|00\rangle$ state in panels (a) and (b)), the details of the electric-field dependence of the Stark shifts can be different. The charge–dipole interaction causes a linear Stark shift of the $|00\rangle$ state at low electric fields, whereas the charge–quadrupole interaction induces a quadratic Stark shift of this state. Panel (c) shows that the simultaneous treatment of the two types of interaction significantly alters the Stark shifts of the rotational states of CO. For example, the $|20\rangle$ state (green line in panels (a)–(c)) is strongly hfs when both the charge–dipole and charge–quadrupole interactions are considered, but not when each of these interactions is considered separately. The reason for this unexpected behavior lies in the fact that the selection rules for the charge–dipole and charge–quadrupole coupling elements in the Stark matrix are different, which can even affect the relative order and signs of the Stark shifts when both interactions are treated simultaneously. In addition, the $|00\rangle$ state exhibits a much more pronounced hfs behavior when both interactions are considered.

Panels (d)–(f) of figure 4 depict the interaction potential between He^+ and CO for an s-wave ($\ell = 0$) collision. The pure Langevin potential $V_L^{(\ell=0)}$ (equation (3)) is displayed in black for comparison. The charge–dipole interaction results in a lfs behavior of the $|10\rangle$ state at low fields (yellow line in panel (a)).

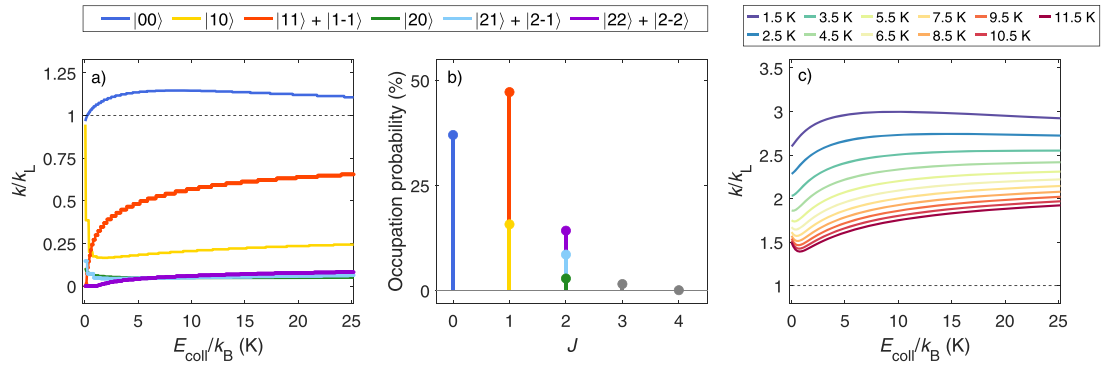

Figure 5. (a) Rotational-state-specific rate coefficients of the $He^+ + CO$ reaction resulting from the combined effects of the charge–dipole and charge–quadrupole interactions, weighted by the probabilities of occupation of the CO $|JM\rangle$ states at $T_{rot} = 6.5$ K displayed in panel (b). (c) Dependence of the state-averaged capture rate coefficient on the value of the CO rotational temperature.

Consequently, the $|10\rangle$ interaction potential has a barrier. In contrast, the $|10\rangle$ state is hfs in the case of the charge–quadrupole interaction (panel (b)) and therefore its interaction potential is more attractive than $V_L^{(\ell=0)}$ (panel (e)). Similarly, the $|11\rangle$-interaction potential is more attractive (repulsive) than $V_L^{(\ell=0)}$ in panel (d) ((e)) because of the hfs (lfs) behavior caused by the charge–dipole (charge–quadrupole) interaction. The combined effects of the charge–dipole and the charge–quadrupole interactions are displayed in panel (f). Some interaction potentials (e.g., the one corresponding to $|22\rangle$, see purple line in panel (f)) display a potential barrier even for $\ell = 0$.

Potential energy barriers result in capture rate coefficients which drop to zero at the lowest collision energies, as illustrated in the collision-energy-dependent state-specific capture rate coefficients $k_i(E_{coll})$ depicted in panels (g)–(i) of figure 4. For example, $k_{|22\rangle}$ (panel (h)) is zero below $\sim k_B \cdot 3$ K as a consequence of the large barrier exhibited by the interaction potential of the $|22\rangle$ state (panel (e)). In contrast, $k_{|00\rangle}$ is enhanced compared to k_L for all calculations, which is a consequence of the fact that any interaction lowers the energy of the ground state.

The contribution of each $k_i(E_{coll})$ to the total capture rate coefficient depends on the rotational-state-population distribution of the CO molecules at the rotational temperature T_{rot} of the supersonic molecular beam. Figure 5(a) displays the rate coefficients for the states with $J \leqslant 2$ and $|M| \leqslant 2$ resulting from the combined effect of the charge-dipole and -quadrupole interactions. Here, the state-specific capture rate coefficients are weighted according to the occupation probability of the rotational levels at the estimated rotational temperature $T_{rot} = 6.5$ K (see section 2) shown in panel (b). At collision energies between $\sim k_B \cdot 2$ K and $\sim k_B \cdot 25$ K, the largest and the second largest rate coefficients correspond to the rotational states $|00\rangle$ (in blue) and $|11\rangle$ (in orange). $k_{|00\rangle}$ and $k_{|11\rangle}$ represent the largest contributions to $k(E_{coll})$ because (i) they are larger than $k_{|10\rangle}$, $k_{|21\rangle}$, and $k_{|22\rangle}$ in this collision-energy range (see panel (i) of figure 4), and (ii) the states $|00\rangle$ and $|11\rangle$ are more populated at $T_{rot} = 6.5$ K. In figure 4(i), the state-specific rate coefficient of $|20\rangle$ is larger than $k_{|00\rangle}$ and $k_{|11\rangle}$ at $E_{coll}/k_B < 2$ K but, because the occupation probability of $|20\rangle$ is less than 3% (green line in figure 5), this state makes a near-zero contribution to the state-averaged capture rate coefficients.

5. Comparison of calculated capture rate coefficients and experimental results

The dependence of the state-averaged capture rate coefficient on the rotational temperature of the CO molecules in the supersonic beam is illustrated in figure 5(c) in the range of T_{rot} between 1.5 K and 11.5 K. Overall, the capture rate coefficient decreases with increasing value of T_{rot} at low collision energies. Below $E_{coll}/k_B = 25$ K, the energy dependence is particularly sensitive to the rotational temperature at low T_{rot} values. Comparing the data presented in figure 5(c) with the experimental data (see figure 3(b)) confirms that the rotational temperature of the CO beam is around 6.5 K.

The blue circles in panels (a)–(c) of figure 6 show the capture rate coefficients calculated considering the charge–dipole interaction, the charge–quadrupole interaction, and both interactions, respectively. The black line results from the convolution of the calculated rate coefficients with Gaussians corresponding to the collision-energy resolution of the measurements, as explained in references [34, 35]. In each panel, the

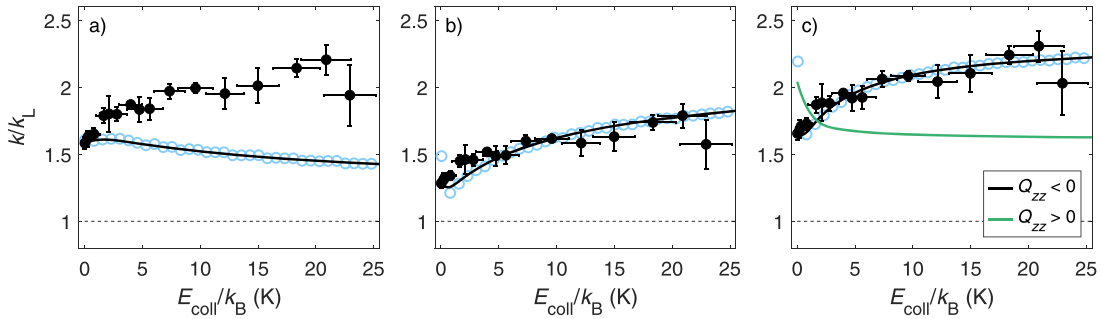

Figure 6. Panels (a)–(c) Comparison of the scaled C^+ ion yield as a function of E_{coll}/k_B (black dots) to the state-averaged capture rate coefficients $k(E_{coll})$ calculated at $T_{rot} = 6.5$ K considering the charge–dipole (a), charge–quadrupole (b), and both interactions (c). The blue circles represent the state-averaged capture rates and the black lines the capture rates obtained by averaging over the distribution of collision energies. The green line corresponds to the rate coefficients calculated assuming the reversed sign of the quadrupole moment of CO (+2.839 D Å). The experimental data have been scaled so as to match the calculated rate coefficients averaged over the experimental collision-energy distribution at $E_{coll}/k_B \approx 0.25$ K.

measured C^+ product yield, already presented in figure 3(b), is also depicted for comparison after scaling by a global factor so that the experimental and calculated values match at the lowest collision energies ($\sim k_B \cdot 0.25$ K).

Common to the three cases is the dominant contribution of the $|00\rangle$ and the $|11\rangle$ states, which are the most populated rotational levels at $T_{rot} = 6.5$ K and lead to rate coefficients which are among the highest (panels (g)–(i) of figure 4). The rates calculated by considering the charge–dipole interaction only (panel (a) of figure 6) exhibit a slight increase of the product yield at low collision energies, which is not observed in the experimental data. The measured decrease in product yield as E_{coll} decreases is well reproduced by the capture rate coefficients calculated considering either the charge–quadrupole interaction only (panel (b)) or both the charge–dipole and the charge–quadrupole interactions (panel (c)). These results indicate that the quadrupole moment determines the E_{coll} dependence of the rates at low collision energies for the reaction between He^+ and CO at $T_{rot} = 6.5$ K, despite the fact that the charge–dipole interaction is of longer range (R^{-2}) than the charge–quadrupole interaction (R^{-3}). Comparison of panels (b) and (c) of figure 6, however, reveals that the inclusion of the charge–dipole interaction has a significant effect on the value of the calculated capture rate coefficient: the inclusion of the ion–dipole interaction increases the capture rate coefficient by about 30% without significantly altering the collision-energy dependence below $k_B \cdot 25$ K.

The blue open circles in panels (b) and (c) reveal a pronounced increase in the capture rate coefficients at very low collision energies, below $\sim k_B \cdot 0.25$ K, caused by the contribution of the $|10\rangle$ level (see yellow line in figure 5). The collision-energy resolution of our measurements is not sufficient for this increase to be observed experimentally. When we average the calculated capture rate coefficients over the distributions of collision energies (black lines in figure 6), this contribution of the $|10\rangle$ state can no longer be observed.

The negative sign of the quadrupole moment of CO is responsible for the observed collision-energy dependence of the rate coefficients of the $He^+ + CO$ reaction. Figure 6 compares the experimental data and the rate coefficients $k(E_{coll})$ calculated considering the actual negative value of Q_{zz} (−2.839 D Å [43]) and a positive value for Q_{zz} (2.839 D Å). The calculations reveal that a positive quadrupole moment of CO would lead to an increase in the product ion yield at $T_{rot} = 6.5$ K as the collision energy decreases below $k_B \cdot 5$ K. This example illustrates that the behavior of the rate coefficients at low collision energies provides information on the sign of the electric quadrupole moment of the neutral molecule.

In previous experimental studies of the $He^+ + CO$ reaction, the thermal reaction rate constant $k(T = 300$ K) was found to be between $0.8k_L$ and $0.97k_L$ [53–56], and Rowe *et al* measured a value of $k(T)$ of $(0.86 \pm 0.26)k_L$ at 8 K (red dot in figure 7). Using the state-specific rate coefficients determined with our capture model including the charge–dipole and the charge–quadrupole interactions, we calculated $k(T)$ in the range between 0 and 25 K by averaging over the populated rotational levels. At 8 K, we obtain a value for $k(T)$ of $1.9k_L$. The results are depicted as black open circles in figure 7 and exhibit a slow decrease with increasing temperature, after an initial rise below 1.1 K. Taking the absolute rate constant determined in reference [57] at 8 K as reference leads to the conclusion that only approximately 45% of the capture processes lead to reaction products. The scaled rate constants are depicted as open orange circles in figure 7. At 300 K, our calculated thermal rate constant approaches k_L. Scaling by 0.45 yields a value of $k(T = 300$ K) that is significantly lower than the measured absolute rates of the reaction at 300 K [53–56]. We have no explanation for this discrepancy. To extract absolute rather than relative rate coefficients from our

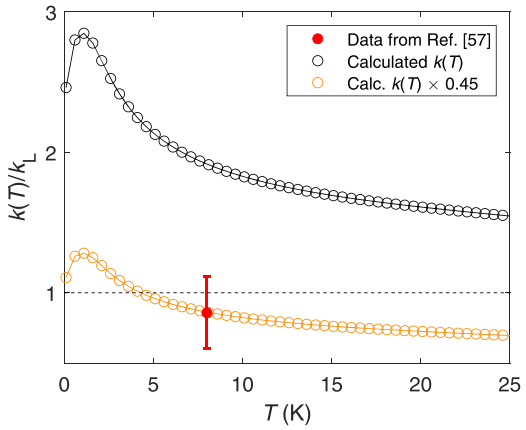

Figure 7. Comparison of the calculated thermal capture rate constant of the $He^+ + CO$ reaction (black open circles) and the $k(T)$-value obtained by Rowe *et al* [57] at $T = 8$ K (red circle with error bar). The orange open circles represent the calculated thermal rate constant $k(T)$ scaled by a factor of 0.45.

measurements, we would need to determine the densities of CO and He(n) reactants in the reaction volume, which presently cannot be done.

6. Conclusions

In this article, we have presented experimental and theoretical investigations of the effects of the electric dipole and quadrupole moments of CO on the rate coefficients of the $He^+ + CO \rightarrow He + C^+ + O$ reaction at collision energies between 0 and $k_B \cdot 25$ K. We used a merged-beam apparatus to study this reaction within the orbit of the helium Rydberg electron and measured the yield of the ionized product C^+ as the collision energy between the reactants was varied. To understand the observed ∼30% decrease in product formation at E_{coll} below $k_B \cdot 5$ K, we employed an adiabatic capture model to calculate the corresponding collision-energy-dependent capture rate coefficients. Our calculations allowed us to identify the CO rotational states $|JM\rangle = |00\rangle$ and $|1 \pm 1\rangle$ as the states with the largest contributions to the total capture rate coefficients because of their large rate coefficients and their high probability of occupation at the rotational temperature $T_{rot} = 6.5$ K of the supersonic CO beam.

Although the charge–quadrupole interaction is of shorter range than the charge–dipole interaction, it is the quadrupole moment of the CO molecule which determines the E_{coll} dependence of the rate coefficient at low collision energies. This effect stems from the large magnitude of the quadrupole moment of CO ($Q_{zz} = -2.839$ D Å [43]) and its small dipole moment ($\mu_{el} = 0.112$ D [42]). Additionally, we verified that the sign of the quadrupole moment strongly influences the collision-energy dependence of the capture rate coefficients. The interaction between the (negative) quadrupole moment of CO and the charge of the approaching He^+ ion causes a decrease of the capture rate coefficients at the lowest collision energies. A similar trend of decreasing capture rate coefficients with decreasing collision energy has been observed in the reaction between He^+ and N_2, which, like CO, has a negative quadrupole moment [40].

Our results also indicate that including the charge–dipole interaction has an effect on the magnitude of the rate coefficients. Finally, comparing thermal rate coefficients calculated by including both charge–dipole and charge–quadrupole interactions with the experimental values of Rowe *et al* [57] suggests that only 45% of the capture processes are reactive. A similar comparison at 300 K indicates a higher percentage of reactive capture processes.

We expect a similar collision-energy dependence of the capture rate coefficients in reactions involving He^+ and $^1\Sigma$ molecules with a negative quadrupole moment and either no dipole moment, such as CO_2, or a comparatively small dipole moment, such as N_2O. In the future, it would be interesting to investigate reactions involving $^2\Pi$ molecules. The electric-field-induced repulsion between the states of opposite parity of each Λ doublet of the rotational levels of these molecules should strongly influence the collision-energy dependence of the capture rate coefficients [28–30, 58]. Studies of the reaction between He^+ and NO, a $^2\Pi$ molecule with non-zero dipole and quadrupole moments, are currently under way in our laboratory.

Acknowledgments

We thank Josef A Agner and Hansjürg Schmutz for technical support. This work is supported financially by the Swiss National Science Foundation (Grant No. 200020B-200478) and by the European Research Council through the ERC advanced grant (Grant No. 743121) under the European Union's Horizon 2020 Research and Innovation Program.

Data availability statement

All data that support the findings of this study are included within the article (and any supplementary files).

ORCID iDs

Fernanda B V Martins https://orcid.org/0000-0002-3338-8246
Valentina Zhelyazkova https://orcid.org/0000-0001-7211-6561
Frédéric Merkt https://orcid.org/0000-0002-4897-2234

References

[1] Bell M T and Softley T P 2009 *Mol. Phys.* **107** 99–132
[2] Balakrishnan N 2016 *J. Chem. Phys.* **145** 150901
[3] Bohn J L, Rey A M and Ye J 2017 *Science* **357** 1002–10
[4] Hu M G, Liu Y, Nichols M A, Zhu L, Quéméner G, Dulieu O and Ni K K 2021 *Nat. Chem.* **13** 435–40
[5] Heazlewood B R and Softley T P 2021 *Nat. Rev. Chem.* **5** 125–40
[6] Wester R 2009 *J. Phys. B: At. Mol. Opt. Phys.* **42** 154001
[7] Markus C R, Asvany O, Salomon T, Schmid P C, Brünken S, Lipparini F, Gauss J and Schlemmer S 2020 *Phys. Rev. Lett.* **124** 233401
[8] Willitsch S 2017 *Adv. Chem. Phys.* **162** 307–40
[9] Allmendinger P, Deiglmayr J, Schullian O, Höveler K, Agner J A, Schmutz H and Merkt F 2016 *Chem. Phys.* **17** 3596–608
[10] Langevin P 1905 *Ann. Chim. Phys.* **T5** 245–88
[11] Ausloos P (ed) 1979 *Kinetics of Ion–Molecule Reactions* (*Nato Advanced Study Institute Series B: Physics* vol 40) (Berlin: Springer)
[12] Bowers M 1979 *Gas Phase Ion Chemistry* (New York: Academic)
[13] Baer M and Ng C Y (ed) 1992 *State-Selected and State-To-State Ion–Molecule Reaction Dynamics: II. Theory* (*Advances in Chemical Physics* vol 82) (New York: Wiley)
[14] Clary D C 1985 *Mol. Phys.* **54** 605–18
[15] Troe J 1987 *J. Chem. Phys.* **87** 2773–80
[16] Vogt E and Wannier G H 1954 *Phys. Rev.* **95** 1190–8
[17] Fabrikant I I and Hotop H 2001 *Phys. Rev.* A **63** 022706
[18] Dashevskaya E I, Litvin I, Nikitin E E and Troe J 2005 *J. Chem. Phys.* **122** 184311
[19] Gao B 2013 *Phys. Rev.* A **88** 022701
[20] Dashevskaya E I, Litvin I, Nikitin E E and Troe J 2016 *J. Chem. Phys.* **145** 244315
[21] Clary D C 1990 *Annu. Rev. Phys. Chem.* **41** 61–90
[22] Troe J 1996 *J. Chem. Phys.* **105** 6249–62
[23] Auzinsh M, Dashevskaya E I, Litvin I, Nikitin E E and Troe J 2013 *J. Chem. Phys.* **139** 084311
[24] Auzinsh M, Dashevskaya E I, Litvin I, Nikitin E E and Troe J 2013 *J. Chem. Phys.* **139** 144315
[25] Smith S C and Troe J 1992 *J. Chem. Phys.* **97** 5451–64
[26] Dashevskaya E I, Litvin I, Nikitin E E and Troe J 2004 *J. Chem. Phys.* **120** 9989–97
[27] Hall F H J and Willitsch S 2012 *Phys. Rev. Lett.* **109** 233202
[28] Wickham A G, Stoecklin T S and Clary D C 1992 *J. Chem. Phys.* **96** 1053–61
[29] Wickham A G and Clary D C 1993 *J. Chem. Phys.* **98** 420
[30] Auzinsh M, Dashevskaya E I, Litvin I, Nikitin E E and Troe J 2008 *J. Chem. Phys.* **128** 184304
[31] Klippenstein S J, Georgievskii Y and McCall B J 2010 *J. Phys. Chem.* A **114** 278–90
[32] Sanz-Sanz C, Aguado A, Roncero O and Naumkin F 2015 *J. Chem. Phys.* **143** 234303
[33] Allmendinger P, Deiglmayr J, Agner J A, Schmutz H and Merkt F 2014 *Phys. Rev.* A **90** 043403
[34] Zhelyazkova V, Martins F B V, Agner J A, Schmutz H and Merkt F 2020 *Phys. Rev. Lett.* **125** 263401
[35] Zhelyazkova V, Martins F B V, Agner J A, Schmutz H and Merkt F 2021 *Phys. Chem. Chem. Phys.* **23** 21606–22
[36] Allmendinger P, Deiglmayr J, Höveler K, Schullian O and Merkt F 2016 *J. Chem. Phys.* **145** 244316
[37] Höveler K, Deiglmayr J, Agner J A, Schmutz H and Merkt F 2021 *Phys. Chem. Chem. Phys.* **23** 2676–85
[38] Höveler K, Deiglmayr J and Merkt F 2021 *Mol. Phys.* **119** e1954708
[39] Merkt F, Höveler K and Deiglmayr J 2022 *J. Phys. Chem. Lett.* **13** 864–71
[40] Zhelyazkova V, Martins F B V, Žeško M and Merkt F 2022 *Phys. Chem. Chem. Phys.* **24** 2843
[41] Martins F B V, Zhelyazkova V, Seiler C and Merkt F 2021 *New J. Phys.* **23** 095011
[42] Nelson R D Jr, Lide D R Jr and Maryott A A 1967 Selected values of electric dipole moments for molecules in the gas phase *Tech. Rep. 10*
[43] Graham C, Imrie D A and Raab R E 1998 *Mol. Phys.* **93** 49–56
[44] Jankunas J, Bertsche B, Jachymski K, Hapka M and Osterwalder A 2014 *J. Chem. Phys.* **140** 244302
[45] Shagam Y, Klein A, Skomorowski W, Yun R, Averbukh V, Koch C P and Narevicius E 2015 *Nat. Chem.* **7** 921–6
[46] Zhelyazkova V, Žeško M, Schmutz H, Agner J A and Merkt F 2019 *Mol. Phys.* **117** 2980–9

[47] Hollenstein U et al 2001 Chimia 55 759–62
[48] Wiley W C and McLaren I H 1955 Rev. Sci. Instrum. 26 1150–7
[49] Olney T N, Cann N M, Cooper G and Brion C E 1997 Chem. Phys. 223 59–98
[50] Bogaard M P, Buckingham A D, Pierens R K and White A H 1978 J. Chem. Soc. Faraday Trans. 74 3008–15
[51] Wong S S M 1998 Introductory Nuclear Physics (New York: Wiley)
[52] Zare R N 1988 Angular Momentum (New York: Wiley)
[53] Anicich V G, Laudenslager J B, Huntress W T Jr and Futrell J H 1977 J. Chem. Phys. 67 4340–50
[54] Lindinger W, Albritton D L and Fehsenfeld F C 1975 J. Chem. Phys. 62 4957–8
[55] Bolden R C, Hemsworth R S, Shaw M J and Twiddy N D 1970 J. Phys. B: At. Mol. Phys. 3 45–60
[56] Fehsenfeld F C, Schmeltekopf A L, Goldan P D, Schiff H I and Ferguson E E 1966 J. Chem. Phys. 44 4087–94
[57] Rowe B R, Marquette J B, Dupeyrat G and Ferguson E E 1985 Chem. Phys. Lett. 113 403–6
[58] Auzinsh M, Dashevskaya E I, Litvin I, Nikitin E E and Troe J 2009 J. Chem. Phys. 130 014304